

Multilayer WS₂ for low-power visible and near-infrared phototransistors

Aniello Pelella¹ · Kimberly Intonti^{2,3} · Ofelia Durante² · Arun Kumar² · Loredana Viscardi^{2,3} · Sebastiano De Stefano² · Paola Romano^{1,3} · Filippo Giubileo³ · Hazel Neill⁴ · Vilas Patil⁴ · Lida Ansari⁴ · Brendan Roycroft⁴ · Paul K. Hurley^{4,5} · Farzan Gity⁴ · Antonio Di Bartolomeo^{2,3}

Received: 16 January 2024 / Accepted: 18 March 2024

Published online: 25 March 2024

© The Author(s) 2024 [OPEN](#)

Abstract

Mechanically exfoliated multilayer WS₂ flakes are used as the channel of field effect transistors for low-power photodetection in the visible and near-infrared (NIR) spectral range. The electrical characterization as a function of the temperature reveals devices with n-type conduction and slightly different Schottky barriers at the drain and source contacts. The WS₂ phototransistors can be operated in self-powered mode, yielding both a current and a voltage when exposed to light. The spectral photoresponse in the visible and the NIR ranges shows a high responsivity (4.5 μA/W) around 1250 nm, making the devices promising for telecommunication applications.

1 Introduction

Among van der Waals layered materials, transition metal dichalcogenides (TMDs) have recently gained attention from the scientific community for their peculiar optoelectronic characteristics [1–5]. Indeed, TMDs exhibit a unique combination of atomic-scale thickness, direct bandgap, strong spin–orbit coupling and favorable electronic and mechanical properties [6–9], which make them interesting for fundamental studies as well as for applications in energy harvesting [10, 11], optoelectronics [12–17], spintronics [18], data storage [19, 20], synaptic devices [21, 22], flexible devices [23–27], etcetera.

Tungsten disulphide (WS₂) belongs to the family of TMDs and presents a layered hexagonal crystal structure, with layers held together by van der Waals forces. Due to the weak interlayer interactions, WS₂ crystals can be easily exfoliated mechanically by scotch tape [28, 29]. The WS₂ monolayer consists of three atomic planes in which the W atomic plane is sandwiched between two planes of S atoms, forming the S–W–S structure, and has a thickness of ~0.625 nm [30]; moreover, it is free from dangling bonds, with stable and nonreactive surface [31].

Like in other semiconducting TMDs, the WS₂ band structure depends on the number of layers. The 1.3 eV bandgap of the bulk widens up to 2.1 eV in the monolayer [32] and a transition from indirect to direct bandgap is observed [33]. The direct bandgap enhances the photoluminescence (PL) that in the monolayer is more than three orders of magnitude stronger than in the bulk [34, 35]. Conversely, multilayer WS₂ is advantageous for photodetection due to increased optical absorption and carrier mobility [36].

✉ Antonio Di Bartolomeo, adibartolomeo@unisa.it | ¹Department of Science and Technology, University of Sannio, Via De Sanctis 59/A, 82100 Benevento, Italy. ²Department of Physics “E. R. Caianiello”, University of Salerno, Via Giovanni Paolo II, 84084 Fisciano, Salerno, Italy. ³CNR-SPIN Salerno, Via Giovanni Paolo II, 84084 Fisciano, Italy. ⁴Tyndall National Institute, University College Cork, Lee Maltings, Dyke Parade, Cork T12 R5CP, Ireland. ⁵School of Chemistry, University College Cork, Cork, Ireland.



The excellent electronic and optical properties of WS_2 have already been exploited in optoelectronic devices [9, 37, 38] like photodetectors, LEDs, lasers, and optical modulators [39–45]. Following the trend, in the present work, multilayer WS_2 flakes are used to fabricate broadband phototransistors over Si/SiO_2 substrates. The transistors show excellent field-effect properties with a high electron mobility of $6\text{ cm}^2/Vs$. The devices are tested under a laser light source, which can be tuned in wavelength and power. The extensive photocurrent spectroscopy analysis, performed in the visible (500–700 nm) and near-infrared (1100–1300 nm) range, shows that the devices are promising for optical telecommunications.

2 Materials and methods

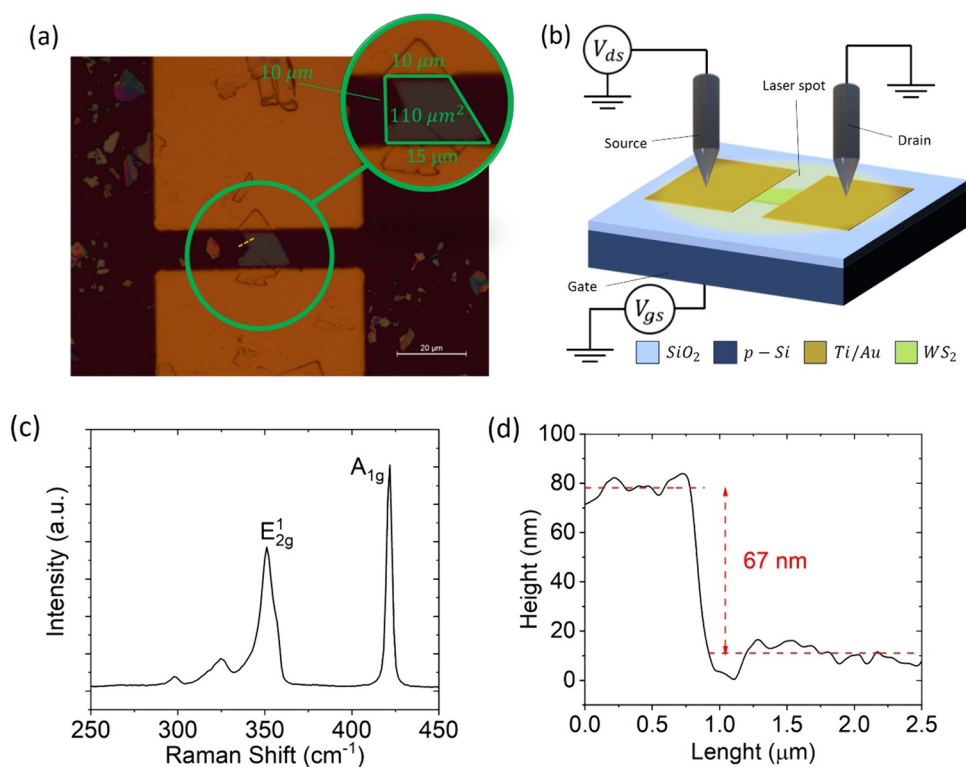
Several WS_2 flakes were transferred by mechanical exfoliation onto a highly doped (resistivity $\rho = 0.001\Omega\text{ cm}$) p-type Si/SiO_2 substrate, with oxide thickness of 85 nm. Then, two Ti/Au (10/100 nm) pads were deposited on top of selected flakes as electrical contacts.

Figure 1a shows an optical image of the device that will be considered in the following. The magnification (green circle) displays the WS_2 flake (highlighted by the green trapezoid), with an optical active area $A_{opt} \approx 110\ \mu\text{m}^2$. Figure 1b presents a schematic of a device and the measurement experimental setup, pointing out that the laser spot (with area $A_{spot} \approx 0.13\text{ mm}^2$), covers the entire device. The Si substrate is the back gate, while the two Ti/Au pads are the source and drain of the transistor. Figure 1c shows the Raman spectrum of the WS_2 flake, measured at room temperature by means of a commercial inVia Renishaw Raman microscope with a Centrus CCD detector with 514 nm laser excitation. The Raman spectrum demonstrates multiple distinct peaks, each corresponding to specific vibrational mode of the crystal lattice. The Raman scattering peaks of the WS_2 flake are located at 421.78 , 351.06 , 324.67 , and 297.58 cm^{-1} , consistent with the reported data [46].

Figure 1d shows the atomic force microscope (AFM) image of the device and the height profile along the line crossing the border of the WS_2 flake (yellow dashed line in Fig. 1a). The step height indicates a thickness of 67 nm, corresponding to about 100 layers.

To get insight into the atomistic structure and electrical characteristics of WS_2 in contact with Ti metal, density functional theory (DFT) and nonequilibrium Green's function (NEGF) have been carried out as implemented in QuantumATK [47, 48]. Linear combination of numerical atomic-orbital basis set and generalized gradient approximation (GGA)

Fig. 1 **a** Optical image of the device under investigation in this study. The area of the flakes is estimated in the green circle to be around $110\ \mu\text{m}^2$. **b** Device and measurements setup schematic. **c** Raman spectroscopy. **d** AFM profile of the device



norm-conserving pseudopotentials from PseudoDojo with medium basis sets [49] are employed in the simulations. Brillouin zone integrations are performed over a grid of k-points generated according to the Monkhorst–Pack scheme [50], with a density of approximately 10 k-points per angstrom. An energy cut-off of 110 Ha is considered for the discretized grid, and all structural relaxation is performed with a maximum force of less than $0.02 \text{ eV } \text{\AA}^{-1}$. For discretized grid, ~ 880 k-point per angstrom have been used for the Green's function calculations, in the direction normal to the Ti/WS₂ interface plane. The metal crystallographic orientation with common supercell with minimal strain for Ti[0001] has been considered for commensurable interface leading to 3.8% strain. The strain arising from the lattice constant mismatch between the materials at the Ti/WS₂ interface has been applied to the metal electrodes, since, unlike WS₂, a few percent in-plane lattice constant of metal surface does not affect its electronic properties considerably [51].

3 Results and discussion

Figure 2a shows the current–voltage (I–V) characteristic of the device under ambient dark condition and with floating gate (i.e. gate electrode not connected to the source-measurement unit). The slightly asymmetric I–V curve suggests the presence of two slightly asymmetric Schottky barriers under drain and source contacts [52]. The drain current (I) as a function of the gate-source voltage (V_g), i.e. the transfer characteristic, for $-50 \text{ V} < V_g < 50 \text{ V}$ and fixed source-drain voltage ($V = 9 \text{ V}$), is reported in Fig. 2b. The transfer characteristic shows an n-type behavior. A wide hysteresis, typical of 2D materials-based transistors and due to intrinsic and extrinsic charge trapping in the channel region [53–57], is observed in the transfer characteristic. The low value of the drain current measured in Fig. 2a indicates that the device was initially on the lower branch of the hysteretic loop. From the forward sweep, the electron mobility can be extracted as:

$$\mu = \left(\frac{dI_d}{dV_g} \right) \frac{L}{CW} \frac{1}{V} = 6 \text{ cm}^2 \text{ V}^{-1} \text{ s}^{-1}$$

where L and W are the length and the width of the channel, and C is the oxide capacitance per unit area ($C = 39 \text{ nF/cm}^2$). Besides, as another figure of merit of the transistor, the subthreshold swing, defined as $SS = \left(\frac{d(\ln(I))}{dV_g} \right)^{-1}$, is evaluated to be 6.5 V/dec.

For a deeper understanding of the transport phenomena, we measured the device I–V characteristics at different temperatures, from 300 to 390 K. Figure 2c show these I–V curves in dark. The device shows that the current increases for increasing temperature, pointing to a conduction dominated by thermionic emission. Indeed, the two Schottky barriers at the contacts make the device behave as two back-to-back diodes. This means that the current is the reverse saturation current of a Schottky diode for both negative and positive drain voltages. Hence, the current is low and strongly dependent on temperature. We can estimate the Schottky barrier heights (SBHs, φ_B) formed at the Ti/WS₂ interface from the current versus temperature behaviour at given drain voltages (here, $V = \pm 0.5 \text{ V}$). The Schottky diode reverse saturation current is expressed as:

$$I_0 = SA^{**} T^2 e^{-\varphi_B/k_b T}$$

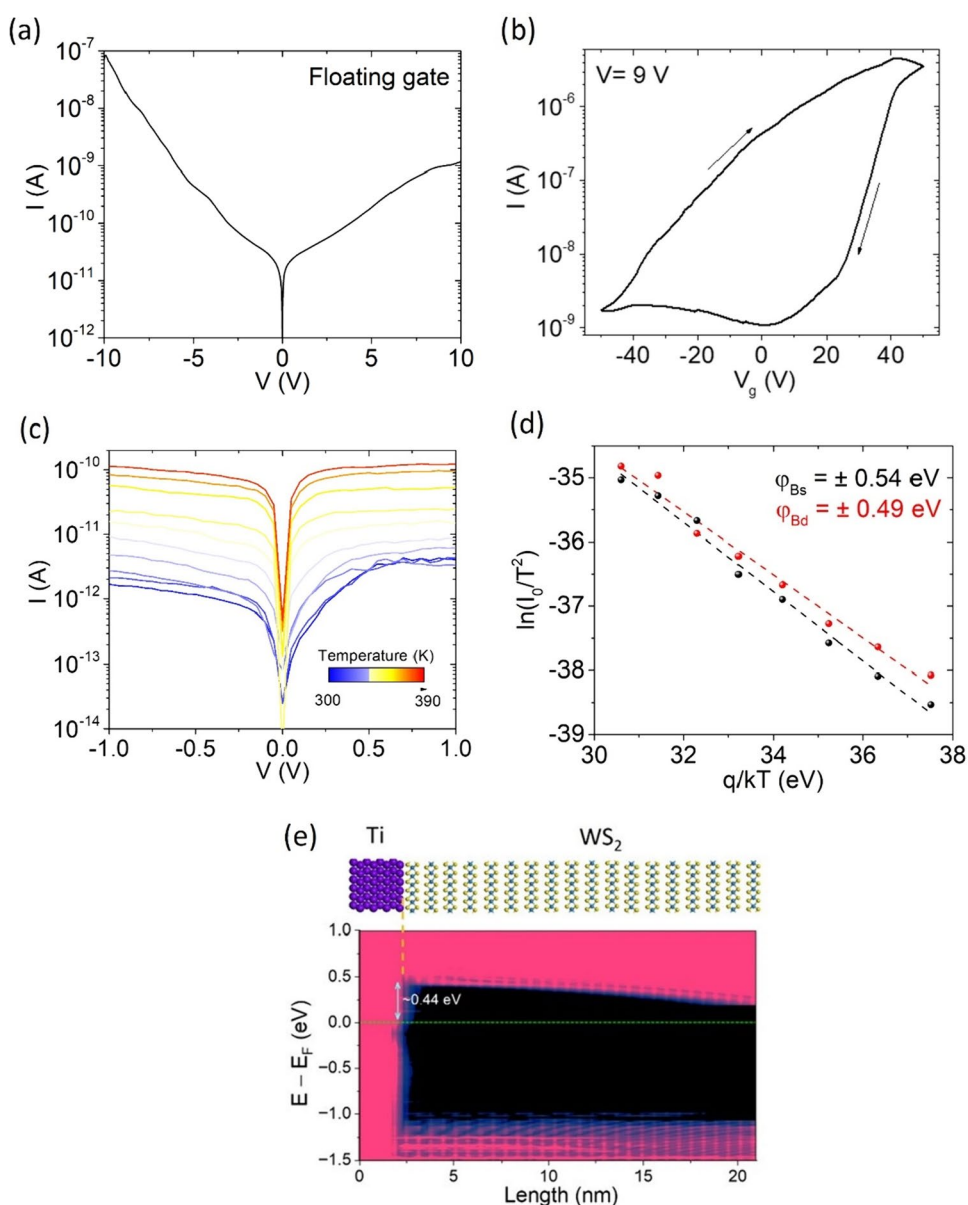
where S is the area of the junction, A^{**} is the effective Richardson constant, k_b is the Boltzmann constant and T is the temperature. The above equation can be rewritten as:

$$\ln(I_0/T^2) = \ln(SA^{**}) - \varphi_B/k_b T$$

from which we can evaluate the SBHs as the slope of the data plotted in Fig. 2d. As expected, the SBHs formed at the drain contact ($\varphi_{Bd} = 0.49 \text{ eV}$) and at the source contact ($\varphi_{Bs} = 0.54 \text{ eV}$) do not differ significantly. The SBH of a metal/semiconductor Schottky junction can be compared with the local density of states (LDoS) along the transport direction [58]. The experimentally extracted SBH at the Ti/WS₂ interface is consistent with our DFT simulations, where a potential barrier of $\sim 0.44 \text{ eV}$ is obtained at the interface (Fig. 2e).

To investigate the photoresponse of the device we exposed it to a white laser source. The I–V characteristics in the dark (black line) and under laser irradiation (red line) are displayed in Fig. 3a. The low value of the dark drain current corresponds to the lower branch of the hysteretic loop (Fig. 2b) and indicates fully depleted channel. When exposed to

Fig. 2 **a** Current–voltage characteristic with floating gate in dark condition. **b** Transfer characteristic at $V = 9\text{ V}$ in dark condition. **c** Current–voltage characteristics as a function of the temperature. **d** Evaluation of the Schottky barrier heights formed under drain and source contacts. **e** Atomic structure (top) and local density of states (LDOS) of the Ti/WS₂ interface (bottom), demonstrating the band offset at the interface



light, the device shows an increased current due to the photoconduction effect. Besides, a left shift is presented under laser irradiation, suggesting that also a photovoltaic effect occurs [59, 60].

As a first approach to the study of the optoelectronic properties of the device, a series of white laser pulses (60 s long) have been sent on the sample. Figure 3b, c show the photoresponse peaks at several applied voltage biases, ranging from -0.5 V to 0.5 V , with steps of 0.1 V . An increasing photocurrent ($I_{ph} = I_{light} - I_{dark}$) is observed for increasing bias voltages.

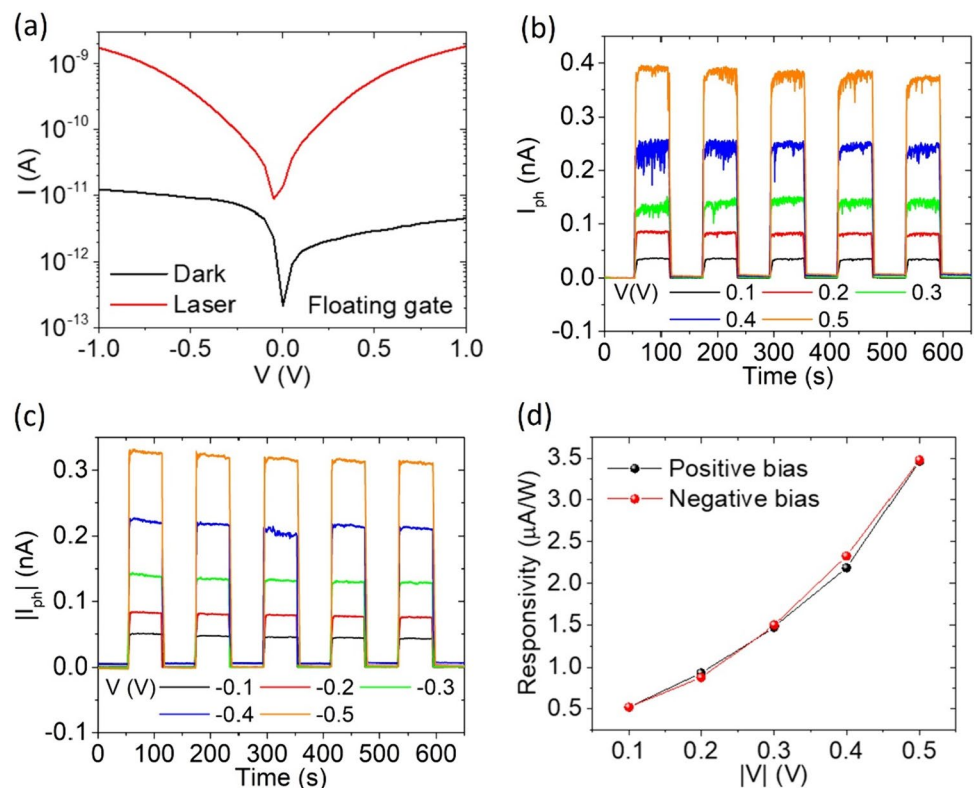
The responsivity (R), which is the most remarkable figure of merit of a photodetector, is defined as the photogenerated current per unit of incident optical power,

$$R = I_{ph}/P_{inc}(\lambda)$$

where $P_{inc}(\lambda) = P(\lambda) \cdot A_{act}/A_{spot}$

The responsivity of the device versus the applied voltage bias is displayed in Fig. 3d. The responsivity shows an increase for increasing drain bias. The voltage dependence of the responsivity is due to enhanced exciton dissociation into free electrons and holes [61] and image-force lowering of the Schottky barrier caused by the increasing in-plane electric field [62, 63].

Fig. 3 **a** Current–voltage characteristic with floating gate in dark (black line) and under laser irradiation. **b, c** Photocurrent peaks and **d** responsivity at different bias voltages



We completed the investigation of the device by testing its operation in self-powered mode. We irradiated the sample with a series of laser pulses (60 s long) without voltage bias (Fig. 4a) or current bias (Fig. 4b). The WS_2 transistor shows a photogenerated current $I_{ph} \approx 4$ pA at $V=0$ V and photogenerated voltage $V_{ph} \approx 8$ mV at $I=0$ A, enabling its use as a self-powered device. The obtained zero-bias photoresponse, which is defined as $\frac{I_{light} - I_{dark}}{I_{dark}}$, is $\approx 2700\%$.

To further understand the photodetection properties of the device, we measured I - V curves at different incident optical powers (Fig. 5a). Figure 5b reports higher responsivity at lower incident power, along with a photocurrent that changes with P_{inc} , following a sub-linear behaviour. The increasing incident optical power leads to an increase in photogenerated charge carriers, which corresponds to an increase in photocurrent. The responsivity, instead, decreases at high incident optical power, when the enhanced carrier density leads to an increase of scattering rate favouring electron–hole recombination and limiting the charge carrier mobility [64, 65].

The peaks in Fig. 5c show a photocurrent which increases with increasing P_{inc} . The photocurrent is due to excitations of electrons from trap states and to the presence of adsorbates, such as O_2 and H_2O , on the WS_2 surface, which are desorbed under light exposure with consequent increase of the WS_2 n-doping level [66].

Fig. 4 **a** Photocurrent at 0 V and **b** photovoltage at 0 A peaks obtained by 60 s laser pulses

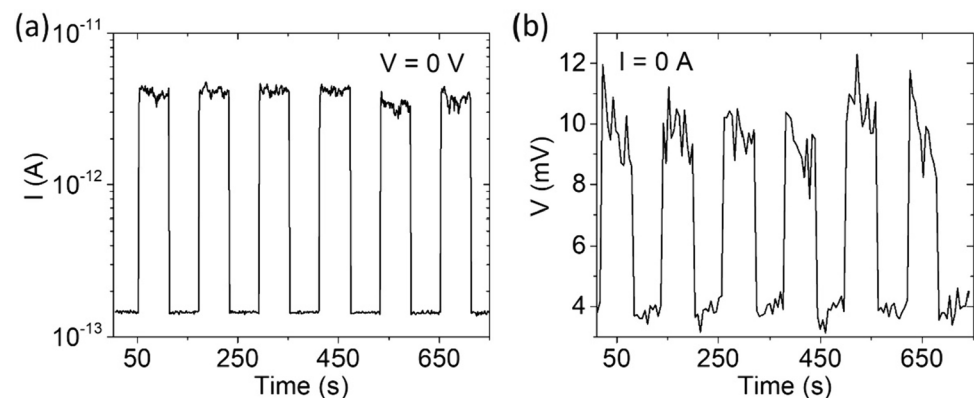
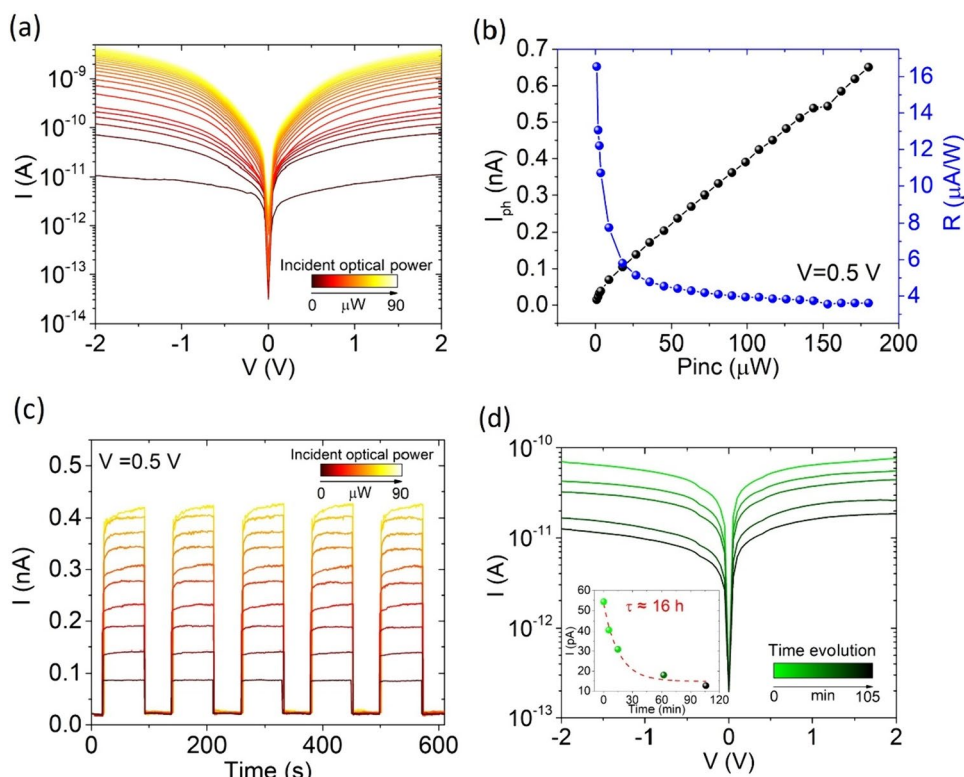


Fig. 5 **a** I–V characteristics at different incident optical powers. **b** Photocurrent and responsivity of the device versus incident optical power. **c** Current peaks at different incident optical power. **d** I–V characteristics in dark measured at successive times. Inset: time evolution of the current extracted at $V=0.5$ V



The graph in Fig. 5d shows the time evolution of the dark current over a time of about 100 min. The inset of Fig. 5d reports the extracted dark current at $V=0.5$ V, which can be fitted by an exponential law, giving a time constant of about 16 h. The slow decay is dominated by the slow photocharge trapping and the adsorption of O_2 and H_2O . The device presents a persistent photoconductivity, which can make it suitable for photonic neuromorphic devices [67].

We also investigated light absorption in the visible and near-infrared (NIR) range. Figure 6a reports I–V characteristics at different wavelengths, from 500 to 700 nm. Furthermore, at given wavelengths, the device was exposed to a series of light pulses yielding the current peaks displayed in Fig. 6b.

The spectral photoresponse reveals a peak at about $\lambda = 590$ nm, corresponding to a photon energy of $E_g = 2.1$ eV (Fig. 6c). Few layers WS_2 shows an indirect band-gap of 1.4 eV and a direct band-gap of 2.1 eV [68], which explains the observed behaviour. The inset of Fig. 6c shows the measured optical absorption spectrum that matches the spectral photoresponse in the visible region [69, 70]. The device shows a responsivity up to $R = 2.2$ $\mu A/W$, along with a specific detectivity [71], defined as $D^* = \sqrt{\frac{A}{2qI_{dark}}} R$, of about $2 \cdot 10^4$ Jones (Fig. 6d).

A similar analysis has been conducted over the NIR range. Figure 7 reports IV characteristics, current peaks, photoresponse, responsivity and specific detectivity at different wavelengths from 1100 to 1400 nm. The absorption spectrum presents the highest peak at about 1250 nm, where the responsivity reaches 4.5 $\mu A/W$ and D^* is $4 \cdot 10^4$ Jones. While the literature does not provide a definitive explanation, the emergence of a peak in the near-infrared region may be attributed to the presence of interlayer excitons. These excitons can exhibit absorbance at lower energies, particularly when the active medium consists of several distinct multilayer flakes [72–74]. Indeed, our channel appears to be made of two (or even more) different flakes, as shown in the optical image of Fig. 1a. The high responsivity in the NIR region makes the device a promising candidate for applications in optical telecommunications.

4 Conclusions

Field effect transistors based on mechanically exfoliated multilayer WS_2 have been studied as photodetectors. Their operation in self-powered mode has been investigated, revealing photo-signals at zero voltage or current biases. Indeed, the WS_2 device shows a photogenerated current $I_{ph} \approx 4$ pA at $V=0$ V and photogenerated voltage $V_{ph} \approx 8$ mV at $I=0$ A.

Fig. 6 **a** I–V characteristics and **b** current peaks varying wavelength in the visible range. **c** Photoresponse, **d** responsivity and external quantum efficiency of the device over the visible wavelength range (500–700 nm). Inset of **c** reports the measured absorption spectrum in the visible wavelength range

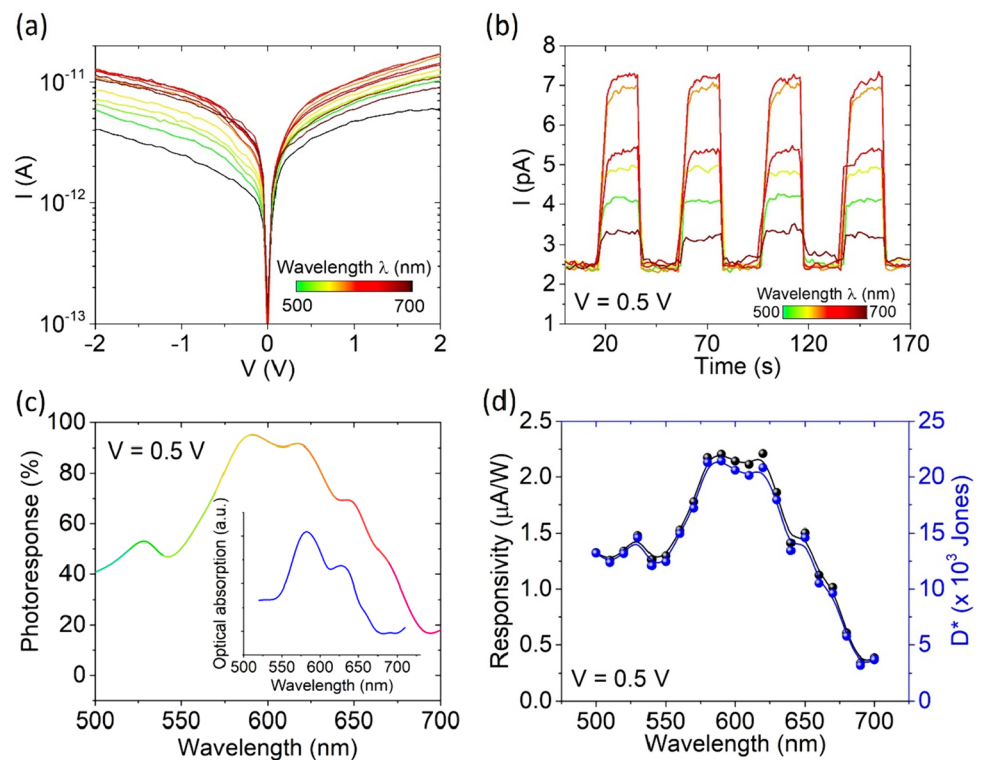
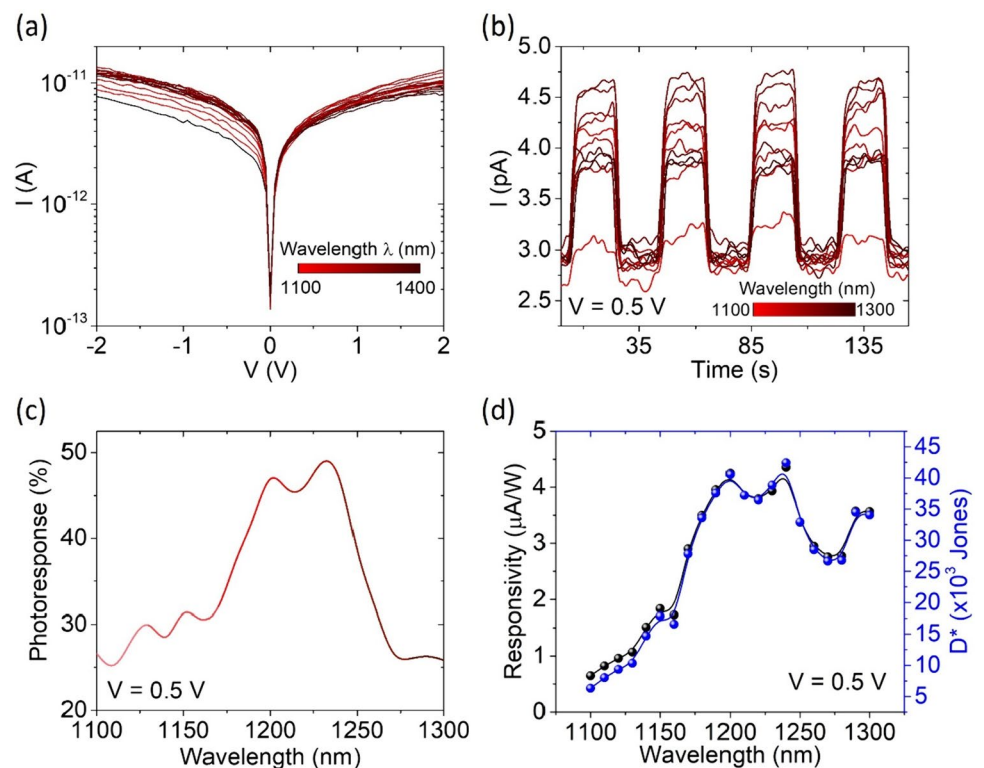


Fig. 7 **a** I–V characteristics and **b** current peaks at different wavelengths in the NIR range. **c** Photoresponse, **d** responsivity and external quantum efficiency of the device over the wavelength NIR range (1100–1300 nm)



Besides, a complete optoelectronic study of the device as a function of the incident laser power has been conducted, revealing higher performances at low incident power. Finally, we studied the photoresponse of the device in both visible and infrared regions, reporting a high responsivity at 1250 nm, paving the way for WS_2 applications in optical telecommunication.

Acknowledgements H.N., V.P., L.A. P.K.H. and F.G. acknowledge the financial support from Science Foundation Ireland AMBER Research Centre (SFI-12/RC/2278_P2). H.N. also acknowledges funding through Irish Research Council (IRC) EPSPG/2023/1772 project. The SFI/HEA Irish Centre for High-End Computing (ICHEC) is acknowledged for the provision of computational facilities and support.

Author contributions A.P. wrote the main manuscript text. A.D.B., F.Gity., and P.K.H. reviewed and edited the manuscript. A.P., K.I., L.V., and B.R. prepared figures 2-7. V.P., O.D., S.D.S prepared Figure 1. All Authors contributed to the formal analysis. L.A., F. Gity, F. Giubileo, P.R. performed numerical simulations. O.D., S.D.S., and L.V. performed data curation. All authors reviewed the manuscript. A.P., K.I., A.K., P.R., B.R. and F.Giubileo. performed data acquisition. V.P., L.A., H.N, and F.Gity. prepared the samples. A.D.B., F. Gity, and P.K.H. performed project administration and supervision.

Data availability Data sets generated during the current study are available from the corresponding author on reasonable request.

Declarations

Competing interests The authors declare no competing interests.

Open Access This article is licensed under a Creative Commons Attribution 4.0 International License, which permits use, sharing, adaptation, distribution and reproduction in any medium or format, as long as you give appropriate credit to the original author(s) and the source, provide a link to the Creative Commons licence, and indicate if changes were made. The images or other third party material in this article are included in the article's Creative Commons licence, unless indicated otherwise in a credit line to the material. If material is not included in the article's Creative Commons licence and your intended use is not permitted by statutory regulation or exceeds the permitted use, you will need to obtain permission directly from the copyright holder. To view a copy of this licence, visit <http://creativecommons.org/licenses/by/4.0/>.

References

1. Manzeli S, Ovchinnikov D, Pasquier D, Yazyev OV, Kis A. 2D transition metal dichalcogenides. *Nat Rev Mater*. 2017;2:1–15.
2. Chowdhury T, Sadler EC, Kempa TJ. Progress and prospects in transition-metal dichalcogenide research beyond 2D. *Chem Rev*. 2020;120:12563–91.
3. Joseph S, et al. A review of the synthesis, properties, and applications of 2D transition metal dichalcogenides and their heterostructures. *Mater Chem Phys*. 2023;297:127332.
4. Zhang W, Wang Q, Chen Y, Wang Z, Van der Wee ATS. Waals stacked 2D layered materials for optoelectronics. *2D Mater*. 2016;3:022001.
5. Tajik S, et al. Transition metal dichalcogenides: synthesis and use in the development of electrochemical sensors and biosensors. *Biosens Bioelectron*. 2022;216:114674.
6. Qian Z, Jiao L, Xie L. Phase engineering of two-dimensional transition metal dichalcogenides. *Chin J Chem*. 2020;38:753–60.
7. Bendavid LI, Zhong Y, Che Z, Konuk Y. Strain-engineering in two-dimensional transition metal dichalcogenide alloys. *J Appl Phys*. 2022;132:225303.
8. Huang L, et al. Enhanced light–matter interaction in two-dimensional transition metal dichalcogenides. *Rep Prog Phys*. 2022;85:046401.
9. Grillo A, Passacantando M, Zak A, Pelella A, Di Bartolomeo A. WS₂ nanotubes: electrical conduction and field emission under electron irradiation and mechanical stress. *Small*. 2020;16:2002880.
10. Lei W, Xiao J-L, Liu H-P, Jia Q-L, Zhang H-J. Tungsten disulfide: synthesis and applications in electrochemical energy storage and conversion. *Tungsten*. 2020;2:217–39.
11. Sun C-B, et al. Tungsten disulfide-based nanomaterials for energy conversion and storage. *Tungsten*. 2020;2:109–33.
12. Voshell A, Terrones M, Rana M. Review of optical properties of two-dimensional transition metal dichalcogenides. In *Wide bandgap power and energy devices and applications III vol 10754*. SPIE. 2018, pp. 66–83.
13. Li Q, Meng J, Li Z. Recent progress on Schottky sensors based on two-dimensional transition metal dichalcogenides. *J Mater Chem A*. 2022;10:8107–28.
14. Romeo F, Di Bartolomeo A. The experimental demonstration of a topological current divider. *Nat Commun*. 2023;14:3709.
15. Wu M, et al. Synthesis of two-dimensional transition metal dichalcogenides for electronics and optoelectronics. *InfoMat*. 2021;3:362–96.
16. Pelella A, et al. Two-dimensional α -In₂Se₃ field effect transistor for wide-band photodetection and non-volatile memory. *J Phys Chem Solids*. 2023;183:111653.
17. Intonti K, et al. Temperature-dependent conduction and photoresponse in few-layer ReS₂. *ACS Appl Mater Interfaces*. 2023;15:50302–11.
18. Gilardoni CM, Hendriks F, van der Wal CH, Guimarães MHD. Symmetry and control of spin-scattering processes in two-dimensional transition metal dichalcogenides. *Phys Rev B*. 2021;103:115410.
19. Kumar A, et al. Optoelectronic memory in 2D MoS₂ field effect transistor. *J Phys Chem Solids*. 2023;179:111406.
20. Sleziona S, et al. Manipulation of the electrical and memory properties of MoS₂ field-effect transistors by highly charged ion irradiation. *Nanoscale Adv*. 2023;5:6958–66.
21. Luo Z-D, et al. Artificial optoelectronic synapses based on ferroelectric field-effect enabled 2D transition metal dichalcogenide memristive transistors. *ACS Nano*. 2020;14:746–54.
22. Wang S, Zhang DW, Zhou P. Two-dimensional materials for synaptic electronics and neuromorphic systems. *Sci Bull*. 2019;64:1056–66.
23. Pataniya PM, Patel V, Sumesh CK. MoS₂/WSe₂ nanohybrids for flexible paper-based photodetectors. *Nanotechnology*. 2021;32:315709.
24. Pataniya P, et al. Paper-based flexible photodetector functionalized by WSe₂ nanodots. *ACS Appl Nano Mater*. 2019;2:2758–66.

25. Zheng Z, et al. Flexible, transparent and ultra-broadband photodetector based on large-area WSe₂ film for wearable devices. *Nanotechnology*. 2016;27:225501.
26. Pataniya PM, et al. Low-temperature Raman investigations and photoresponse of a detector based on high-quality WSe₂ crystals. *J Phys Chem C*. 2020. <https://doi.org/10.1021/acs.jpcc.9b08381>.
27. Zheng Z, Yao J, Yang G. Centimeter-scale deposition of Mo_{0.5}W_{0.5}Se₂ alloy film for high-performance photodetectors on versatile substrates. *ACS Appl Mater Interfaces*. 2017;9:14920–8.
28. Ding J, et al. Properties, preparation, and application of tungsten disulfide: a review. *J Phys D Appl Phys*. 2021;54:173002.
29. Lan C, Li C, Ho JC, Liu Y. 2D WS₂: from vapor phase synthesis to device applications. *Adv Electron Mater*. 2021;7:2000688.
30. Liu W, Cao W, Kang J, Banerjee K. (Invited) High-performance field-effect-transistors on monolayer-WSe₂. *ECS Trans*. 2013;58:281.
31. Romanov RI, et al. Thickness-dependent structural and electrical properties of WS₂ nanosheets obtained via the ALD-grown WO₃ sulfurization technique as a channel material for field-effect transistors. *ACS Omega*. 2021;6:34429–37.
32. Gusakova J, et al. Electronic properties of bulk and monolayer TMDs: theoretical study within DFT framework (GVJ-2e method). *Phys Status Solidi A*. 2017;214:1700218.
33. Park J, Kim MS, Cha E, Kim J, Choi W. Synthesis of uniform single layer WS₂ for tunable photoluminescence. *Sci Rep*. 2017;7:16121.
34. Gutiérrez HR, et al. Extraordinary room-temperature photoluminescence in triangular WS₂ monolayers. *Nano Lett*. 2013;13:3447–54.
35. Han C, Wang Y, Zhou W, Liang M, Ye J. Strong anisotropic enhancement of photoluminescence in WS₂ integrated with plasmonic nanowire array. *Sci Rep*. 2021;11:10080.
36. Yao JD, Zheng ZQ, Shao JM, Yang GW. Stable, highly-responsive and broadband photodetection based on large-area multilayered WS₂ films grown by pulsed-laser deposition. *Nanoscale*. 2015;7:14974–81.
37. Niknam S, Dehdast SA, Pourdakan O, Shabani M, Koohi MK. Tungsten disulfide nanomaterials (WS₂ NM) application in biosensors and nanomedicine: a review. *Nanomed Res J*. 2022;7:214–26.
38. Khurajam A, Kumar V, Halder N, Mukhopadhyay AK. Memristive and biological synaptic behavior in transition metal dichalcogenide-WS₂ nanostructures: a review. *Mater Today Proc*. 2022;62:1585–90.
39. Huang L, et al. Monolayer WS₂ based electro-absorption modulator. *Opt Mater*. 2021;113:110851.
40. Yang S, et al. CMOS-compatible WS₂-based all-optical modulator. *ACS Photon*. 2018;5:342–6.
41. Zhang C, et al. High-performance photodetectors for visible and near-infrared lights based on individual WS₂ nanotubes. *Appl Phys Lett*. 2012;100:243101.
42. Li J, Han J, Li H, Fan X, Huang K. Large-area, flexible broadband photodetector based on WS₂ nanosheets films. *Mater Sci Semicond Process*. 2020;107:104804.
43. Gao W, et al. 2D WS₂ based asymmetric Schottky photodetector with high performance. *Adv Electron Mater*. 2021;7:2000964.
44. Kim BH, Yoon H, Kwon SH, Kim DW, Yoon YJ. Direct WS₂ photodetector fabrication on a flexible substrate. *Vacuum*. 2021;184:109950.
45. Durante O, et al. Multiwalled WS₂ nanotubes on interdigitated electrodes for visible-light photodetectors. In 2023 IEEE nanotechnology materials and devices conference (NMDC); 2023. pp. 676–680. <https://doi.org/10.1109/NMDC57951.2023.10343680>.
46. Berkdemir A, et al. Identification of individual and few layers of WS₂ using Raman spectroscopy. *Sci Rep*. 2013;3:1755.
47. Smidstrup S, et al. QuantumATK: an integrated platform of electronic and atomic-scale modelling tools. *J Phys Condens Matter*. 2019;32:015901.
48. Zhussupbekov K, et al. Revealing the influence of edge states on the electronic properties of PtSe₂. *Appl Mater Today*. 2023;35:101926.
49. van Setten MJ, et al. The PseudoDojo: training and grading a 85 element optimized norm-conserving pseudopotential table. *Comput Phys Commun*. 2018;226:39–54.
50. Monkhorst HJ, Pack JD. Special points for Brillouin-zone integrations. *Phys Rev B*. 1976;13:5188–92.
51. Bokdam M, Brocks G, Katsnelson MI, Kelly PJ. Schottky barriers at hexagonal boron nitride/metal interfaces: a first-principles study. *Phys Rev B*. 2014;90:085415.
52. Grillo A, Di Bartolomeo A. A current–voltage model for double Schottky barrier devices. *Adv Electron Mater*. 2021;7:2000979.
53. Di Bartolomeo A, et al. Hysteresis in the transfer characteristics of MoS₂ transistors. *2D Materials*. 2017;5:015014.
54. Kaushik N, et al. Reversible hysteresis inversion in MoS₂ field effect transistors. *Npj 2D Mater Appl*. 2017;1:34.
55. Datye IM, et al. Reduction of hysteresis in MoS₂ transistors using pulsed voltage measurements. *2D Mater*. 2018;6:011004.
56. Intonti K, et al. Hysteresis and photoconductivity of few-layer ReSe₂ field effect transistors enhanced by air pressure. *Adv Elect Mater*. 2023;9:2300066.
57. Urban F, et al. Gas dependent hysteresis in MoS₂ field effect transistors. *2D Mater*. 2019;6:045049.
58. Greer JC, Blom A, Ansari L. Properties of homo- and hetero-Schottky junctions from first principle calculations. *J Phys Condens Matter*. 2018;30:414003.
59. Yoo HB, et al. Modeling and characterization of photovoltaic and photoconductive effects in insulated-gate field effect transistors under optical excitation. *Solid-State Electron*. 2021;186:108139.
60. Cui M, et al. Photoconductive and photovoltaic metal-semiconductor-metal κ-Ga₂O₃ solar-blind detectors with high rejection ratios. *J Phys D Appl Phys*. 2022;55:394003.
61. Massicotte M, et al. Dissociation of two-dimensional excitons in monolayer WSe₂. *Nat Commun*. 2018;9:1633.
62. Deylgat E, Chen E, Fischetti MV, Sorée B, Vandenberghe WG. Image-force barrier lowering in top- and side-contacted two-dimensional materials. *Solid-State Electron*. 2022;198:108458.
63. Di Bartolomeo A, et al. Asymmetric Schottky contacts in bilayer MoS₂ field effect transistors. *Adv Func Mater*. 2018;28:1800657.
64. Bhattacharya P. *Semiconductor optoelectronic devices*. 2nd ed. New York: Prentice-Hall Inc; 1997.
65. Banerjee JP, Banerjee S. *Physics of semiconductors and nanostructures*. Boca Raton: CRC Press; 2019.
66. Di Bartolomeo A, et al. Temperature-dependent photoconductivity in two-dimensional MoS₂ transistors. *Mater Today Nano*. 2023;4:100382.
67. Lee M, et al. Brain-inspired photonic neuromorphic devices using photodynamic amorphous oxide semiconductors and their persistent photoconductivity. *Adv Mater*. 2017;29:1700951.

68. Kuc A, Zibouche N, Heine T. Influence of quantum confinement on the electronic structure of the transition metal sulfide TS_2 . *Phys Rev B*. 2011;83:245213.
69. Jiao H, et al. HgCdTe/black phosphorus van der Waals heterojunction for high-performance polarization-sensitive midwave infrared photodetector. *Sci Adv*. 2022;8:1811.
70. Wu S, et al. Ultra-sensitive polarization-resolved black phosphorus homojunction photodetector defined by ferroelectric domains. *Nat Commun*. 2022;13:3198.
71. Shin GH, et al. Si-MoS₂ vertical heterojunction for a photodetector with high responsivity and low noise equivalent power. *ACS Appl Mater Interfaces*. 2019;11:7626–34.
72. Tan Q, et al. Layer-engineered interlayer excitons. *Sci Adv*. 2021;7:863.
73. Ovesen S, et al. Interlayer exciton dynamics in van der Waals heterostructures. *Commun Phys*. 2019;2:1–8.
74. Zheng S, et al. Coupling and interlayer exciton in twist-stacked WS₂ bilayers. *Adv Opt Mater*. 2015;3:1600–5.

Publisher's Note Springer Nature remains neutral with regard to jurisdictional claims in published maps and institutional affiliations.